Fragmentation of a Magnetized Filamentary Molecular Cloud Rotating around its Axis

Tomoaki Matsumoto, Fumitaka Nakamura, and Tomoyuki Hanawa Department of Astrophysics, School of Science, Nagoya University, Chikusa-ku, Nagoya, Aichi, 464-01

> E-mail(TM) matsu@a.phys.nagoya-u.ac.jp (Received 1993 July 26; Accepted 1994 February 9)

Abstract

The dynamical instability of a self-gravitating magnetized filamentary cloud was investigated while taking account of rotation around its axis. The filamentary cloud of our model is supported against self-gravity in part by both a magnetic field and rotation. The density distribution in equilibrium was assumed to be a function of the radial distance from the axis, $\rho_0(r) = \rho_c (1 + r^2/8H^2)^{-2}$, where ρ_c and H are model parameters specifying the density on the axis and the length scale, respectively; the magnetic filed was assumed to have both longitudinal (z-) and azimuthal $(\varphi$ -) components with a strength of $B_0(r) \propto \sqrt{\rho_0(r)}$. The rotation velocity was assumed to be $v_{0\varphi} = \Omega_{\rm c} r (1 + r^2/8H^2)^{-1/2}$. We obtained the growth rate and eigenfunction numerically for (1) axisymmetric (m = 0) perturbations imposed on a rotating cloud with a longitudinal magnetic field, (2) non-axisymmetric (m=1) perturbations imposed on a rotating cloud with a longitudinal magnetic filed, and (3) axisymmetric perturbations imposed on a rotating cloud with a helical magnetic field. The fastest growing perturbation is an axisymmetric one for all of the model clouds studied. Its wavelength is $\lambda_{\rm max} \leq 11.14\,H$ for a non-rotating cloud without a magnetic field, and is shorter when the magnetic filed is stronger and/or the rotation is faster. For a rotating cloud without a magnetic filed the most unstable axisymmetric mode is excited mainly by self-gravity (the Jeans instability), while the unstable non-axisymmetric mode is excited mainly by non-uniform rotation (the Kelvin-Helmholtz instability). The unstable non-axisymmetric perturbation corotates with a fluid at r = 2 - 4H and grows in time. When the equilibrium magnetic field is helical, the unstable perturbation grows in time and propagates along the axis. A rotating cloud with a helical magnetic field is less unstable than that with a longitudinal magnetic field.

Key words: Instabilities — Interstellar: magnetic field — Magnetohydrodynamics — Rotation — Stars: formation

to appear in Publications of Astronomical Society of Japan (vol.46, No.3)

1. Introduction

Recent observations have revealed that many molecular clouds contain elongated filamentary structures. These filamentary clouds have dense cores as their internal constituents. Most of the young stellar objects seem to be associated with dense cores. The evolution, i.e., fragmentation, of a filamentary cloud, is therefore interesting in relation to the early phase of star-formation processes.

Filamentary molecular clouds are often associated with magnetic fields which are perpendicular to the cloud in the Taurus region (Moneti et al. 1984) and parallel to the cloud in the Ophiuchus region (Vrba et al. 1976). It has been suggested that the Orion A cloud has helical magnetic fields around the cloud axis (Bally 1989; Uchida et al. 1991). In some filamentary molecular clouds the velocity gradient has a component perpendicular to the filament axis, which can be interpreted as rotation around the axis (see, e.g., Olano et al. 1988; Uchida et al. 1991; Tatematsu et al. 1993). The energies of the magnetic field and the rotation are likely to be comparable to the gravitational energy. These magnetic fields and rotation may influence the fragmentation of the filamentary clouds.

Since the early work of Chandrasekhar and Fermi (1953), the linear stability of a cylindrical gas cloud has been investigated extensively by Stodołkiewicz (1963), Hansen et al. (1976), Nagasawa (1987), Inutsuka and Miyama (1992), and Nakamura et al. (1993, referred to as Paper I in the following). These studies have taken account of the effects of magnetic fields, the stiffness of the equation of state, the rotation and the collapse of the filamentary cloud in the radial direction. However, the stability of a rotating magnetized filamentary cloud against fragmentation has not been discussed. Among the studies referred to above, only Hansen et al. (1976) took into account the rotation around the axis; however, they considered neither the magnetic fields nor the fragmentation in the z-direction. We extend the model of Paper I to include rotation around the axis and to discuss the fragmentation of a rotating filamentary cloud with longitudinal or helical magnetic fields.

The model and computation methods are described in section 2. In section 3 a rotating filamentary cloud with longitudinal magnetic fields is shown to be unstable against axisymmetric and non-axisymmetric perturbations. In section 4 the stability of a rotating filamentary cloud with helical magnetic fields is discussed. In section 5 we discuss the application of our stability analysis and compare our result to the Kelvin-Helmholtz and Balbus-Hawley instabilities.

2. Model and Computation Methods

2.1. Equilibrium Model

As a model of a filamentary molecular cloud, we considered an infinitely long cylindrical gas cloud in equilibrium in which the density and the magnetic field are uniform along the z - axis in a cylindrical coordinate system (r, φ, z) . The model of Paper I was extended so as to include

rotation around the filamentary axis. See, e.g., Bonnell et al. (1992) concerning rotation around an arbitary axis. They followed the fragmentation of a rotating finite-length cloud using numerical simulations.

The hydrostatic equilibrium of a filamentary molecular cloud is described by

$$\frac{dP_0}{dr} + \frac{d}{dr} \left(\frac{B_{0\varphi}^2 + B_{0z}^2}{8\pi} \right) + \frac{B_{0\varphi}^2}{4\pi r} + \rho_0 \left(\frac{v_{0\varphi}^2}{r} + \frac{d\psi_0}{dr} \right) = 0 \tag{1}$$

and

$$\frac{1}{r}\frac{d}{dr}\left(r\frac{d\psi_0}{dr}\right) = 4\pi G\rho_0. \tag{2}$$

Here, P, ρ , v_{φ} , ψ , G, B_{φ} , and B_z are the gas pressure, density, φ -component of the velocity, gravitational potential, gravitational constant, and φ - and z-components of the magnetic field, respectively. Subscript 0 denotes the quantities in the unperturbed state. The magnetic field of the r-component is assumed to vanish in the unperturbed state, $\mathbf{B}_0 = (0, B_{0\varphi}, B_{0z})$. For simplicity, the filamentary gas cloud is assumed to be isothermal,

$$P_0/\rho_0 = c_s^2 = \text{const.} \tag{3}$$

A solution satisfying equations (1) through (3) is expressed as

$$\rho_0 = \rho_c \left(1 + \frac{r^2}{8H^2} \right)^{-2}, \tag{4}$$

$$\mathbf{v}_0 = (0, v_{0\varphi}, 0) = \left\{ 0, r\Omega_{\rm c} \left(1 + r^2 / 8H^2 \right)^{-1/2}, 0 \right\},$$
 (5)

$$\mathbf{B}_0 = (0, B_{0\varphi}, B_{0z}) \,, \tag{6}$$

$$B_{0\varphi} = B_{\rm c} \sin \theta \frac{r}{2\sqrt{2}H} \left(1 + \frac{r^2}{8H^2}\right)^{-3/2},$$
 (7)

$$B_{0z} = B_{\rm c} \left(1 + \frac{r^2}{8H^2} \right)^{-3/2} \sqrt{1 + \cos^2 \theta \frac{r^2}{8H^2}} , \tag{8}$$

and

$$\psi_0 = 8\pi G \rho_c H^2 \ln \left(1 + \frac{r^2}{8H^2} \right), \tag{9}$$

where

$$4\pi G \rho_{\rm c} H^2 = c_{\rm s}^2 + \frac{B_{\rm c}^2}{16\pi\rho_{\rm c}} (1 + \cos^2 \theta) + 2\Omega_{\rm c}^2 H^2. \tag{10}$$

All of the symbols with subscript c denote the values at r=0. The effective radius of this model is $r=2\sqrt{2}H$.

The density distribution of our model is the same as those of Stodółkiewicz (1963), Ostriker (1964), Nagasawa (1987), and Paper I. Among these models, our solution is the most general in the sense that our model incorporates rotation around the axis as well as helical and longitudinal

magnetic fields. Our solution has five model parameters: ρ_c , c_s , B_c , θ , and Ω_c . The θ parameter denotes the ratio of the φ - and z-components of the magnetic fields and is equal to the pitch angle of the magnetic fields at $r=\infty$, $\theta=\lim_{r\to\infty}\tan^{-1}(B_{0\varphi}/B_{0z})$. When $\Omega_c=0$, our model reduces to that of Paper I. When $\theta=0$ and $\Omega_c=0$, the magnetic field is parallel to the filament axis and the model reduces to that of Stodółkiewicz's (1963) solution for clouds with longitudinal magnetic fields. When $B_c=0$, our solution reduces to Ostriker's (1964) isothermal solution for non-magnetized clouds. The sign of B_c is taken to be positive in this paper unless otherwise noted. In this equilibrium model, the ratios of the magnetic and centrifugal forces to the gas pressure (α and β) are spatially constant:

$$\alpha \equiv \frac{B_{0\varphi}^2 + B_{0z}^2}{8\pi P_0} = \frac{B_c^2}{8\pi \rho_c c_s^2} = \text{const}$$
 (11)

and

$$\beta \equiv \frac{2\Omega_{\rm c}^2 H^2}{c_{\rm s}^2} = \text{const.}$$
 (12)

The condition for equilibrium [equation (10)] thus reduces to

$$4\pi G\rho_{\rm c}H^2 = c_{\rm s}^2 \left[1 + \alpha \left(\frac{1 + \cos^2 \theta}{2} \right) + \beta \right] . \tag{13}$$

In the following we take H as the unit of length and $(2\pi G\rho_c)^{-1/2}$ as the unit of time. The model can thus be specified by three non-dimensional parameters: α , β , and θ . In the subsequent sections we investigate the dependence of the growth rate on α , β , and θ .

2.2. Perturbation Equations

We considered a perturbation of a small amplitude superimposed on the equilibrium cloud described above. The linearized equation of motion for the perturbation is given by

$$\rho_0 \left\{ \frac{\partial \boldsymbol{v}_1}{\partial t} + (\boldsymbol{v}_0 \cdot \nabla) \boldsymbol{v}_1 + (\boldsymbol{v}_1 \cdot \nabla) \boldsymbol{v}_0 \right\} - \frac{\boldsymbol{j}_0 \times \boldsymbol{B}_1 + \boldsymbol{j}_1 \times \boldsymbol{B}_0}{c} + \nabla P_1 + \rho_1 \nabla \psi_0 + \rho_0 \nabla \psi_1 = 0,$$
(14)

where v and $j = (c/4\pi)\nabla \times B$ are the velocity and electric current density, respectively; all of the symbols with subscript 1 denote the changes in the quantities due to the perturbation. The equation of continuity, the Poisson equation, and the induction equation are respectively expressed as follows:

$$\frac{\partial \rho_1}{\partial t} + \nabla \cdot (\rho_0 \boldsymbol{v}_1 + \rho_1 \boldsymbol{v}_0) = 0, \qquad (15)$$

$$\Delta \psi_1 = 4\pi G \rho_1 \tag{16}$$

and

$$\frac{\partial \boldsymbol{B}_1}{\partial t} = \nabla \times (\boldsymbol{v}_1 \times \boldsymbol{B}_0 + \boldsymbol{v}_0 \times \boldsymbol{B}_1) . \tag{17}$$

The perturbation is assumed to be isothermal,

$$P_1 = c_{\rm s}^2 \rho_1 \,. \tag{18}$$

We obtained the normal-mode solutions of equations (14) through (18), in which all of the physical quantities change according to the form

$$\rho_1(r,\varphi,z,t) = \rho_1(r)\exp(-i\omega t + im\varphi + ik_z z). \tag{19}$$

After some manipulation of equations (14) through (18), it can be rewritten as

$$\frac{d}{dr} \begin{pmatrix} y_1 \\ y_2 \\ y_3 \\ y_4 \end{pmatrix} = \begin{pmatrix} A_{11} & A_{12} & A_{13} & A_{14} \\ A_{21} & A_{22} & A_{23} & 0 \\ 0 & 0 & 0 & A_{34} \\ A_{41} & A_{42} & A_{43} & A_{44} \end{pmatrix} \begin{pmatrix} y_1 \\ y_2 \\ y_3 \\ y_4 \end{pmatrix},$$
(20)

where

$$(y_1, y_2, y_3, y_4) = \left(P_1 + \frac{B_{1\varphi}B_{0\varphi} + B_{1z}B_{0z}}{4\pi}, \frac{i\rho_0 v_{1r}}{\omega}, \rho_c \psi_1, \rho_c g_{1r}\right). \tag{21}$$

The symbol $g_{1r}(=d\psi_1/dr)$ denotes the change in the gravitational acceleration in the r-direction. The elements of matrix A are given explicitly in appendix 1.

The boundary conditions were set so that the perturbation is regular at r=0 and infinitesimal at $r=\infty$. Since the perturbation equation is singular at r=0, we obtained regular solutions near to r=0 according to the method of Paper I. The asymptotic solutions in the region $r\gg 4H$ were also obtained according to Paper I.

2.3. Numerical Procedure

The eigenvalues and eigenfunctions were obtained essentially with the methods of Paper I. Namely, we integrated the perturbation equation both from r=0 and ∞ for a given $\omega (= \omega_r + i\omega_i)$ and checked whether the integrated solutions could be connected continuously at a middle point. When a solution satisfied the boundary conditions at r=0 and ∞ for a given ω , we regarded the given ω as beeing an eigenvalue.

We searched for eigenvalues using the bisection method. When $\Omega = 0$ or $m = \theta = 0$, the eigenvalue (ω^2) is always real and can be obtained by the usual bisection method. When otherwise, we extended the bisection method for a complex eigenvalue. The technical details concerning the extended bisection method are given in appendix 2.

Equation (20) has a singularity at $v_{0\varphi} = r\omega_r/m$ when $m \neq 0$. The result depends on the integration path (see, e.g., Lin 1945a, b; Kato 1987). We integrated equation (20) over r along the real axis. This integration path is correct only for unstable modes. Although this integration path is not correct for damped modes, we applied it for simplicity, since we are not much interested in damped modes.

3. Rotating Clouds with Longitudinal Magnetic Fields

In this section we consider the stability of a rotating cloud with longitudinal magnetic fields. The parameter θ is fixed to be 0° in this section, except where otherwise stated.

3.1. Sausage (m = 0) Mode

In the beginning we consider the sausage mode (m = 0) instability of a rotating nonmagnetized filamentary cloud. The eigenvalue (ω) is purely imaginary for the unstable mode. Figure 1 shows the dispersion relation for the model of $(\alpha, \beta) = (0, 1)$ by the thick curve. The abscissa and ordinate are the non-dimensional wavenumber $(k_z H)$ and the non-dimensional growth rate $(\omega_i/\sqrt{2\pi G\rho_c})$, respectively. There is only one unstable sausage mode for the models with $\alpha = 0$, although there are some unstable sausage modes for $\alpha > 0$ (Paper I). The sausage mode is unstable only when the wavenumber is smaller than a critical one, $k_{z, cr}H = 0.960$. The growth rate has its maximum, $\omega_{i,\text{max}} = 0.606 \sqrt{2\pi G \rho_c}$, at $k_z H = 0.467$. The dashed and thin curves denote the growth rate of the most unstable mode for $(\alpha, \beta) = (0, 0)$ and $(\alpha, \beta) = (1, 0)$, respectively. The rotation as well as the longitudinal magnetic fields increase the maximum growth rate $(\equiv \omega_{i, \max})$, the wavenumber of the fastest growing perturbation $(\equiv k_{z, \max})$, and the critical wavenumber ($\equiv k_{z,cr}$). This is because both rotation around the axis and longitudinal magnetic fields support the gas against gravity in the radial direction, but does not operate in the z-direction. The gas temperature is lower for fixed ρ_c and H when α and β are larger [see equation (10). Accordingly the Jeans length, the typical length scale for fragmentation due to self-gravity, is shorter. The wavenumber of the fastest growing perturbation is almost the same for $(\alpha, \beta) = (0, 1)$ and (1, 0). This implies that $k_{z, \text{max}}$ is a function of c_s for $\theta = 0^\circ$. The maximum growth rate is smaller for $(\alpha, \beta) = (0, 1)$ than for $(\alpha, \beta) = (1, 0)$. This means that the Parker instability increases the growth rate when a magnetic field is present.

Figure 2 shows the dependence of the growth rate on β for $\alpha = 0$. As β increases, $\omega_{i, \text{max}}$, $k_{z, \text{max}}$, and $k_{z, \text{cr}}$ increase. The wavenumber of the fastest growing perturbation can be approximated by

$$k_{z, \max} H = 0.72 \left[(1 + \alpha + \beta)^{1/3} - 0.6 \right]$$
 (22)

for $\theta=0^\circ$. Figure 3 shows the accuracy of equation (22). The upper panel shows $k_{z,\,\text{max}}$ as a function of $\alpha+\beta$. Equation (22) is drawn by the curve and the numerically obtained values $(k_{z,\,\text{max}})$ are plotted with filled circles. The lower panel shows the deviation from equation (22). Equation (22) gives a good estimate for $k_{z,\,\text{max}}$ with an error of 2% for $0 \le \alpha+\beta \le 6$. Equation (22) is used for a comparison with a filamentary molecular cloud, Orion A, by Hanawa et al. (1993). See Hanawa et al. (1993) for an application of equation (22). The approximate dispersion relation is given by

$$\omega^{2} = -4\pi G \rho_{c} \frac{k_{z}H}{1 + k_{z}H} \frac{0.89 + 1.4\alpha}{1 + 1.25\alpha} + c_{s}^{2}k_{z}^{2}$$

$$= -4\pi G \rho_{c} \left(\frac{k_{z}H}{1 + k_{z}H} \frac{0.89 + 1.4\alpha}{1 + 1.25\alpha} - \frac{H^{2}k_{z}^{2}}{1 + \alpha + \beta} \right)$$
(23)

for the most unstable sausage mode for all the models of $\theta=0^{\circ}$. The upper and lower expressions of equation (23) are equivalent [see equation (13)]. The second term on the right-hand side of equation (23) denotes the stabilization due to thermal pressure, i.e., the dispersion relation of the sound wave. When α and β are larger, $c_{\rm s}$ is lower, and, accordingly, the growth rate is larger. The maximum growth rate obtained from equation (23) agrees with the numerical results with an error of 5% for $0.5 \le \alpha \le 10$ and $0 \le \beta \le 10$, and for $\alpha = 0$ and $0 \le \beta \le 2$.

Figure 4 shows the fastest growing perturbation for $(\alpha, \beta) = (0, 1)$. The density distribution in the r-z plane is indicated by the grey scale and the velocity field is denoted by arrows. The amplitude of the perturbation is taken to be $\rho_1/\rho_0 = \varepsilon \cos(k_z z)$ at r=0. To emphasize the density contrast we have taken $\varepsilon = 0.65$ in figure 4. The relative density perturbation $(|\rho_1/\rho_0|)$ has its maximum on the axis (r=0). The velocity perturbation is dominant in the z-direction. The velocity perturbation in the z-direction has its maximum, $v_{1z} = -0.941 \varepsilon c_s \sin(k_z z)$, on the axis and monotonically decreases as r increases. The velocity perturbation in the r-direction has its maximum, $v_{1r} = -0.128 \varepsilon c_s \cos(k_z z)$, at r = 2.73 H. The φ -component of the velocity is shown in the right panel. The solid and dashed curves denote the velocity in the perturbed state and in equilibrium, respectively. The change in the rotation velocity is small with a maximum, $v_{1\varphi} = 0.193 \varepsilon c_s \cos(k_z z)$, at r = 1.76 H.

The eigenfunction shown in figure 4 is similar to that of the fastest growing perturbation for a magnetized non-rotating cloud (see figure 8 of Paper I). A filamentary cloud supported in part by either rotation or longitudinal magnetic fields fragments mainly in the z-direction. We expected in Paper I that a disk perpendicular to the rotation axis is formed by the nonlinear growth of the perturbation. Tomisaka (1993) and Nakamura et al. (1993, private communication) showed this by numerical simulations for magnetized filamentary clouds. We also followed the nonlinear evolution of a rotating filamentary cloud with numerical simulations, and confirmed the formation of a small disk perpendicular to the axis. The results of these numerical simulations will be reported in a future paper.

Figure 5 is the same as figure 4, except for $(\alpha, \beta) = (0.5, 0.5)$. The velocity perturbation is dominant in the z-direction. The velocity perturbation in the z-direction has its maximum, $v_{1z} = -0.886 \varepsilon c_{\rm s} \sin{(k_z z)}$, on the axis when $\rho_1/\rho_0 = \varepsilon \cos{(k_z z)}$. The velocity perturbation in the r-direction has its maximum, $v_{1r} = -0.175 \varepsilon c_{\rm s} \cos{(k_z z)}$, at r = 2.87 H. The change in the rotation velocity is at most $v_{1\varphi} = 0.101 \varepsilon c_{\rm s} \cos{(k_z z)}$ at r = 1.63 H. The characteristics of the most unstable sausage mode for $(\alpha, \beta) = (0.5, 0.5)$ are between those for $(\alpha, \beta) = (1, 0)$ and (0, 1), except for the generation of B_{φ} . When $\alpha\beta \neq 0$, the magnetic field is twisted due to a change in the rotation velocity $[B_{1\varphi} = -0.249 \varepsilon \sin{(k_z z)})$ at r = 1.51 H, at most while $B_{0z} = 3.545 (1 + r^2/8H^2)^{-1}$.

3.2. Kink (m = 1) Mode

Rotating filamentary clouds are also unstable against non-axisymmetric perturbations. We found five modes, three of which are pure oscillations ($\omega_i = 0$) for any k_z . The remaining two

modes have complex conjugate eigenfrequencies. Figure 6 shows the dispersion relation of the unstable kink mode (m=1) for $\alpha=0$ and $\beta=1$. The real and imaginary parts of the eigenfrequency are denoted by the dashed and solid curves, respectively. The dispersion relation is symmetric with respect to k_z , i.e., $\omega(-k_z)=\omega(k_z)$. We thus restrict ourselves to $k_z>0$ in the following. The three horizontal dotted lines in the figure denote the angular velocities , Ω , at r=2, $2\sqrt{2}$, and 4,respectively. The unstable modes have a corotation point where the phase velocity coincides with the fluid velocity $[\omega_r/m=\Omega(r)]$. The corotation point is located near to the effective radius, $r=2\sqrt{2}H$, when the growth rate is large. The growth rate is very small $(\omega_i<1\times10^{-4}\sqrt{2\pi G\rho_c})$ in the region $|Hk_z|<0.04$, and large in the region $0.1 \leq Hk_z<0.477$. Because of the analytical and numerical difficulty at the corotation point $[\omega_r=m\Omega(r)]$, we could not find whether $\omega_i=0$ in the region $|Hk_z|\leq0.04$. When k_z is larger than the critical value $(k_z, cr)=0.477H^{-1}$, the growth rate is again small $(\omega_i<10^{-2}\sqrt{2\pi G\rho_c})$.

The mode having m=-1 is physically the same as that having m=1, except for the sign of ω_r . When m=-1, a mode with $\omega_r<0$ becomes unstable and a mode with $\omega_r>0$ is a pure oscillation. Only when the fluid velocity (= Ω) and the phase velocity of the wave (= ω_r/m) have the same sign can the mode be unstable.

Figures 7 and 8 are the same as figure 6, except for $(\alpha, \beta) = (0, 0.5)$ and (0, 2), respectively. The growth rate is larger when β is larger. The non-rotating filamentary cloud without magnetic fields $(\alpha = \beta = 0)$ has two neutrally stable kink modes with positive and negative real frequencies (see also Nagasawa 1987). Only the mode having a corotation point becomes unstable; the other mode remains pure oscillatory. We can thus conclude that this instability is due to the resonance of the wave to the fluid rotation, and, accordingly, is of the Kelvin-Helmholtz type. Note that non-rotating magnetized filamentary clouds are unstable against the kink mode because of the Parker instability (Paper I).

When $|k_z|$ is small, the growth rate is very small (even if it is positive) and the oscillation frequency is almost independent of β . For long-wavelength perturbations v_z has a large amplitude in the region very far from the axis $(r \geq 10\,H)$. For $|k_z| \geq k_{z,\,\mathrm{cr}}$ the growth rate of the kink mode is very small $(\omega_i < 1 \times 10^{-2})$. The critical wavenumber is $Hk_{z,\,\mathrm{cr}} = 0.301,\,0.477,\,\mathrm{and}$ 0.788 for $(\alpha,\,\beta) = (0,\,0.5),\,(0,\,1),\,\mathrm{and}\,(0,\,2),\,\mathrm{respectively}$. The growth rate has its maximum $[\omega_i/\sqrt{2\pi G\rho_c} = 0.0564,\,0.135,\,\mathrm{and}\,0.255]$ at $Hk_z = 0.225,\,0.323,\,\mathrm{and}\,0.478,\,\mathrm{for}\,(\alpha,\,\beta) = (0,\,0.5),\,(0,\,1),\,\mathrm{and}\,(0,\,2),\,\mathrm{respectively}$.

Figure 9 is the same as figure 4, except for the most unstable kink perturbation for $(\alpha, \beta) = (0, 1)$. Figures 9(a) and (b) denote the cross section in the r - z plane and that of z = 0, respectively. The growth rate and wave number are $\omega_i = 0.135 \sqrt{2\pi G\rho_c}$ and $Hk_z = 0.323$, respectively. The amplitude of the perturbation is normalized so that the density perturbation is at most $\rho_1/\rho_0 = 0.5$. When the kink mode is excited, the density ridge is twisted, as can be seen in figure 9.

Figure 10 is the same as figure 6, except for $(\alpha, \beta) = (0.5, 0.5)$. This model is intermediate

between those of $(\alpha, \beta, \theta) = (1, 0, 0^{\circ})$ and $(0, 1, 0^{\circ})$, the former of which is excited by the Parker instability. For a fixed value of $\alpha + \beta$ the kink mode has a larger growth rate when α is larger.

4. Rotating Cloud with Helical Magnetic Fields

In this section we discuss the sausage mode instability of rotating filamentary clouds with helical magnetic fields ($\alpha\beta\theta \neq 0$).

Figure 11 shows the dispersion relation of the most unstable sausage mode for $\theta = 30^{\circ}$, 60° , and 90° , while $\alpha = \beta = 0.5$. The real (figure 11a) and imaginary (figure 11b) parts of the eigenfrequency are shown as a function of k_z . The sausage mode grows and propagates with a phase speed of ω_r/k_z in the z-direction. The eigenfrequency of the damped mode is the complex conjugate of that of the unstable mode. The eigenfrequency is antisymmetric with respect to k_z , i.e., $\omega(-k_z) = -\omega(k_z)$. The phase velocity is thus always positive for both the unstable and damped modes. When $\theta < 0$, the real part of the eigenfrequency is negative, $\omega_r < 0$. Note that Ω_c is taken to be positive in our computations. The phase velocity is $\omega_r/k_z \simeq 0.025 H\sqrt{2\pi G\rho_c}$ for $\theta = 30^{\circ}$. The phase velocity is faster for a larger θ .

As θ increases, $\omega_{i,\text{max}}$, $k_{z,\text{max}}$, and $k_{z,\text{cr}}$ decrease, and, accordingly, the cloud becomes less unstable. This is due to an increases in the sound speed, c_s , for fixed α and β [see equation (13)]. Both when the magnetic field is longitudinal and helical, the most unstable mode is mainly excited by a self-gravitational instability. The eigenfrequency ω is complex for $\beta\theta \neq 0$, while it is pure imaginary or real for $\beta\theta = 0$. The perturbation therefore grows in time and propagates in the z-direction only when the cloud rotates and is threaded by a helical magnetic field.

Figure 12 shows the fastest growing perturbation for $(\alpha, \beta, \theta) = (0.5, 0.5, 60^{\circ})$. Figure 12 is similar to figure 5, except for the phase shift in the z-direction. The density perturbation is proportional to $\rho_1 \propto \cos(k_z z - \omega_r t + \delta_\rho)$, where the phase shift, δ_ρ , is a function of r, and is taken to be $\delta_\rho = 0$ at r = 0. The phase shift is large for the azimuthal components of the velocity and magnetic fields, e.g., $v_{1\varphi} = 0.141 \varepsilon \cos(k_z z - \omega_r t + 0.561)$ at r = 1.73 H and $B_{1\varphi} = 0.682\varepsilon \sin(k_z z - \omega_r t + 0.356)$ at r = 1.25 H. The upper panel of figure 12 shows the z-dependence of $v_{1\varphi}$ (the dashed curve) at r = 1.73 H and $B_{1\varphi}$ (the solid curve) at r = 1.25 H, both of which have their maximum amplitudes there.

The phase shifts are related to the propagation of the wave. Consider a velocity perturbation proportional to $v_{1r} \propto \cos{(k_z z)}$ and $v_{1z} \propto \sin{(k_z z)}$. The velocity perturbation changes v_{φ} and B_{φ} according to the azimuthal components of the equation of motion and the induction equation. When $\theta = 0$, the changes in the azimuthal components have the dependence $B_{1\varphi} \propto \sin{(k_z z)}$ and $v_{1\varphi} \propto \cos{(k_z z)}$ (see section 3). When $\beta = 0$, they have the dependence $B_{1\varphi} \propto \cos{(k_z z)}$ and $v_{1\varphi} \propto \sin{(k_z z)}$ (see Paper I). When $\beta\theta \neq 0$, both types of the above-mentioned perturbations are produced. These changes in v_{φ} and B_{φ} modify v_r and v_z according to the equation of motion. As a result, velocity perturbations given by $v_{1r} \propto \sin{(k_z z)}$ and $v_{1z} \propto \sin{(k_z z)}$ are also induced and the velocity perturbations apparently propagate.

5. Discussion

As shown in the previous sections, a rotating magnetized filamentary cloud suffers from various instabilities. This is in part because our model includes rotation as well as magnetic fields as well as the self-gravity of the gas. In this section we discuss the relationship between our model and other theoretical studies conserning the instability of a rotating gas cloud. In the last paragraph we also discuss the application of our model to TMC 1 (Taurus Molecular Cloud 1).

5.1. Relationship to the Kelvin-Helmholtz Instability and the Balbus-Hawley Mechanism

Since the angular velocity is non-uniform in our model, we suppose that the Kelvin-Helmholtz instability may be involved in the stability of our model cloud. As discussed by Glatzel (1987a,b), the resonant interaction of two neutral modes produces a couple of growing and damped modes and causes an angular momentum transfer across the corotation point. These characteristics are shared with the unstable kink mode for a rotating cloud without a magnetic field. As shown in subsection 3.2, the growing and damped modes appear in pairs. We confirmed that the angular momentum is transferred from the region inside the corotation point to that outside the corotation point when the unstable kink mode is excited. In the growing mode, ρ_1 and $v_{1\varphi}$ are anti-correlated $(\rho_1^* \cdot v_{1\varphi} < 0)$ inside the corotation point and are positively correlated $(\rho_1^* \cdot v_{1\varphi})$ outside the corotation point, where ρ_1^* denotes the complex conjugate of ρ_1 . This means that the central region loses angular momentum and the outer part receives it. The angular-momentum transfer produces an energy excess, which causes the perturbation to grow.

The energy excess due to the angular momentum transfer is proportional to the difference in the angular velocity across the corotation point. Correspondingly, the growth rate of the Kelvin-Helmholtz instability is bounded by the angular velocity gradient, $\omega_i \leq \max |(1/2)rd\Omega/dr|$ (Sung 1974; Hanawa 1986, 1987; Fujimoto 1987), when the self-gravity of the gas and magnetic fields are negligibly small. In our model, the angular velocity gradient,

$$r\frac{d\Omega}{dr} = -\Omega_{\rm c} \frac{r^2}{8H^2} \left(1 + \frac{r^2}{8H^2}\right)^{-3/2},\tag{24}$$

has its maximum, $0.385 \Omega_c$ at r=4H, and a somewhat smaller value $0.355 \Omega_c$ at the effective radius, $r=2\sqrt{2}H$. It may be not a chance coincidence that the growth rate of the kink mode is large when the angular velocity gradient is large at the corotation point.

The unstable kink mode might be excited in part by another effect related to a large β . When β is large, the sound speed (c_s) and thermal pressure are low [see equation (13)]. The low gas pressure strengthens the effect of the self-gravity relatively and suppresses the Jeans instability less effectively. This effect is appreciable in the axisymmetric mode when $\beta \geq 1$. To investigate this effect on the kink mode, we made an experimental model in which the right-hand side of equation (16) was multiplied by a factor of $0 \leq \varepsilon \leq 1$, $\Delta \psi_1 = 4\pi G \rho_1$. By decreasing ε from unity, the change in the gravitational potential was reduced artificially. As ε decreases, ω_r increases and ω_i decreases. The increase in ω_r is ascribed to a reduction in the self-gravity, since

the self-gravity lowers the propagation of the sound wave. The increase in ω_r shifts the corotation point inwards, and, accordingly, decreases the angular velocity gradient thereof. The decrease in ω_i may be in part due to a decrease in the angular velocity gradient at the corotation point. Thus, unfortunately, we could not decouple the effect of low thermal pressure on the Jeans instability from other effects of large β .

When $\alpha\beta \neq 0$, the unstable sausage mode is in part due to the Balbus-Hawley (1991) mechanism, although it is mainly due to the Jeans instability. Balbus and Hawley showed that a differentially rotating disk is highly unstable if it is threaded by a vertical magnetic filed. In such a disk, an outwardly displaced fluid element tries to enforce a rigid rotation, and thus rotates too fast for its new radial location. Then, the excess centrifugal force drives the element still faster outward. As can be seen in subsection 3.1, the unstable sausage mode generates B_r and B_{φ} . The twisted magnetic fields transfer angular momentum along the field line. We confirmed that the fluid element displaced inward loses angular momentum due to magnetic drag when the unstable sausage mode is excited for $\alpha\beta \neq 0$. Because of the angular momentum gain, the fluid element contracts further due to a decrease in the centrifugal force. In order to evaluate the contribution of the Balbus-Hawley mechanism to the unstable sausage mode, we again computed the artificial models in which the change in the gravitational potential was attenuated by a factor of ε . The growth rate, ω_i , decreases along with a decrease in ε , and diminishes at $\varepsilon = 0$. We thus conclude that the unstable sausage mode is excited mainly by self-gravity. When $\varepsilon = 0$, the increase in the magnetic pressure near to the axis (r=0) stabilizes our model cloud against the Balbus-Hawley mechanism for m=0. We confirmed that the sausage mode is stabilized against the Parker instability by the same mechanism for $(\alpha, \beta) = (1, 0)$ when $\varepsilon = 0$.

5.2. Comparison with Habe et al.'s Simulation

Here, we comment on the collapse of a self-gravitating cloud triggered by torsional Alfvén Waves. Habe et al. (1991) showed by a numerical simulation that a cloud with helical magnetic fields collapse more easily than one with longitudinal magnetic fields. In their simulation, helical magnetic fields are generated by rotation and cause a rotating cloud to collapse due to magnetic pinching. It seems as if our stability analysis contradicts their simulation, since a rotating cloud with helical magnetic fields is less unstable than that with longitudinal magnetic fields in our analysis. The apparent contradiction comes from a difference in the initial models. While our initial model is in equilibrium, Habe et al's (1991) started their numerical simulation from a cloud threaded by helical magnetic fields. Their initial model is not in equilibrium. And our stability analysis cannot be applied directly to their initial model.

5.3. Application to TMC 1

Finally, we discuss the application of our model to a filamentary molecular cloud. TMC 1 contains 5 dense cores which are more or less regularly spaced with an average separation of 4'. Since the apparent diameter is 2', the ratio of the average separation to the filament diameter

is estimated to be ≈ 2 . Substituting this value into our model, we obtain $Hk_{\rm max} \simeq 0.63$. This means that the magnetic and/or centrifugal forces are comparable to the gravitational force $(\alpha + \beta \approx 1)$. This is consistent with the velocity structure of TMC 1. Olano et al. (1988) found a velocity gradient across the filament axis, which can be interpreted as rotation around the axis. The rotation velocity is comparable to the velocity dispersion. This implies that the cloud is supported against gravity in part by rotation, and that the centrifugal force is as strong as the turbulent pressure, $(\beta \approx 1)$.

The authors thank Professors Takenori Nakano and Satoshi Yamamoto for discussions and comments. This work is financially supported in part by the Grant-in-Aid for General Scientific Research (05640308).

Appendix 1. The Matrix Elements of A

Matrix A is expressed as

$$\frac{d}{dr}\mathbf{y} = \mathbf{A}\mathbf{y},\tag{25}$$

$$(y_1, y_2, y_3, y_4) = \left(P_1 + \frac{\mathbf{B}_0 \cdot \mathbf{B}_1}{4\pi}, \frac{i\rho_0 v_{1r}}{\omega}, \rho_c \psi_0, \rho_c g_0\right),$$
 (26)

$$A = R + S T^{-1}U, (27)$$

$$\mathbf{R} = \begin{pmatrix} R_{11} & R_{12} & R_{13} & R_{14} \\ R_{21} & R_{22} & R_{23} & 0 \\ 0 & 0 & 0 & 1 \\ R_{41} & 0 & R_{43} & R_{44} \end{pmatrix}, \tag{28}$$

$$R_{11} = \frac{1}{c_{\rm s}^2} \left(\frac{v_{0\varphi}^2}{r} - g_0 \right) + \frac{2v_{0\varphi}}{r\xi} \frac{m}{r}, \tag{29}$$

$$R_{12} = \omega \xi - \frac{(\mathbf{k} \cdot \mathbf{B}_0)^2}{4\pi \rho_0} \frac{\omega}{\xi}$$
(30)

$$-\frac{2v_{0\varphi}}{r}\frac{\omega}{\xi}\left[\frac{1}{r}\frac{d}{dr}(rv_{0\varphi}) + \frac{\mathbf{k}\cdot\mathbf{B}_0}{4\pi\rho_0}\frac{1}{\xi}\frac{1}{r}\frac{d}{dr}(rB_{0\varphi})\right],\tag{31}$$

$$R_{13} = \frac{2v_{0\varphi}}{r\xi} \frac{m}{r} \frac{\rho_0}{\rho_c},$$

$$R_{14} = -\frac{\rho_0}{\rho_c},$$
(32)

$$R_{14} = -\frac{\rho_0}{\rho_c},\tag{33}$$

$$R_{21} = -\frac{1}{c_{s}^{2}} \frac{\xi}{\omega} + \frac{|\mathbf{k}|^{2}}{\omega \xi},$$

$$R_{22} = -\frac{1}{r} - \frac{\mathbf{k} \cdot \mathbf{B}_{0}}{4\pi \rho_{0}} \frac{1}{\xi^{2}} \left[\frac{m}{r} \frac{1}{r} \frac{d}{dr} (rB_{0\varphi}) + k_{z} \frac{dB_{0z}}{dr} \right]$$
(34)

$$-\frac{m}{r}\frac{1}{\xi}\frac{1}{r}\frac{d}{dr}(rv_{0\varphi}),\tag{35}$$

$$R_{23} = \frac{|\mathbf{k}|^2}{\omega \xi} \frac{\rho_0}{\rho_c},\tag{36}$$

$$R_{41} = \frac{4\pi G \rho_{c}}{c_{s}^{2}},$$

$$R_{43} = |\mathbf{k}|^{2},$$

$$R_{44} = -\frac{1}{r},$$
(37)
(38)

$$R_{43} = |\mathbf{k}|^2, \tag{38}$$

$$R_{44} = -\frac{1}{r}, (39)$$

$$\mathbf{S} = \begin{pmatrix} S_{11} & S_{12} \\ S_{21} & S_{22} \\ 0 & 0 \\ S_{41} & S_{42} \end{pmatrix},\tag{40}$$

$$S_{11} = -\left[\frac{1}{2\pi r} + \frac{1}{4\pi c_{s}^{2}} \left(\frac{v_{0\varphi}^{2}}{r} - g_{0}\right)\right] B_{0\varphi} - \frac{2v_{0\varphi}}{r\xi} \frac{\mathbf{k} \cdot \mathbf{B}}{4\pi}, \tag{41}$$

$$S_{12} = -\frac{1}{4\pi c_{\rm s}^2} \left(\frac{v_{0\varphi}^2}{r} - g_0 \right) B_{0z}, \tag{42}$$

$$S_{21} = \frac{1}{4\pi c_s^2} \frac{\xi}{\omega} B_{0\varphi} - \frac{m}{r} \frac{1}{\xi \omega} \frac{\mathbf{k} \cdot \mathbf{B}_0}{4\pi}, \tag{43}$$

$$S_{22} = \frac{1}{4\pi c_s^2} \frac{\xi}{\omega} B_{0z} - k_z \frac{1}{\xi \omega} \frac{\mathbf{k} \cdot \mathbf{B}_0}{4\pi}, \tag{44}$$

$$S_{41} = -\frac{G}{c_c^2} B_{0\varphi}, \tag{45}$$

$$S_{42} = -\frac{G}{c_s^2} B_{0z}, (46)$$

$$T = \begin{pmatrix} T_{11} & T_{12} \\ T_{21} & T_{22} \end{pmatrix}, \tag{47}$$

$$T_{11} = T_{22} = \frac{B_{0\varphi}B_{0z}}{4\pi\rho_0c_s^2},\tag{48}$$

$$T_{12} = 1 + \frac{B_{0z}^2}{4\pi\rho_0 c_s^2} - \frac{(\mathbf{k} \cdot \mathbf{B}_0)^2}{4\pi\rho_0 \xi^2}, \tag{49}$$

$$T_{21} = 1 + \frac{B_{0\varphi}^2}{4\pi\rho_0 c_s^2} - \frac{(\mathbf{k} \cdot \mathbf{B}_0)^2}{4\pi\rho_0 \xi^2}, \tag{50}$$

$$U = \begin{pmatrix} U_{11} & U_{12} & U_{13} & 0 \\ U_{21} & U_{22} & U_{23} & 0 \end{pmatrix}, \tag{51}$$

$$U_{11} = \frac{B_{0z}}{c_{\rm s}^2 \rho_0} - k_z \frac{\mathbf{k} \cdot \mathbf{B}_0}{\rho_0 \xi^2}, \tag{52}$$

$$U_{12} = \left(\frac{B_{0z}}{\rho_0} \frac{d\rho_0}{dr} - \frac{dB_{0z}}{dr}\right) \frac{\omega}{\rho_0 \xi} + \frac{\omega (\mathbf{k} \cdot \mathbf{B}_0)^2}{4\pi \rho_0^2 \xi^3} \frac{dB_{0z}}{dr}, \tag{53}$$

$$U_{13} = -k_z \frac{\mathbf{k} \cdot \mathbf{B}_0}{\varepsilon^2 \rho_c}, \tag{54}$$

$$U_{21} = \frac{B_{0\varphi}}{c_{\circ}^2 \rho_0} - \frac{m \, \mathbf{k} \cdot \mathbf{B}_0}{r \, \rho_0 \xi^2}, \tag{55}$$

$$U_{22} = \left(\frac{B_{0\varphi}}{\rho_0} \frac{d\rho_0}{dr} - \frac{dB_{0\varphi}}{dr} + \frac{B_{0\varphi}}{r}\right) \frac{\omega}{\rho_0 \xi} + \frac{\omega (\mathbf{k} \cdot \mathbf{B}_0)^2}{4\pi \rho_0^2 \xi^3} \frac{1}{r} \frac{d}{dr} (rB_{0\varphi})$$
 (56)

$$+\frac{\omega}{\rho_0} \mathbf{k} \cdot \mathbf{B}_0 \left[\frac{1}{\xi^2} \left(\frac{dv_{0\varphi}}{dr} + \frac{v_{0\varphi}}{r} \right) - \frac{1}{\omega^2} \left(\frac{dv_{0\varphi}}{dr} - \frac{v_{0\varphi}}{r} \right) \right], \tag{57}$$

$$U_{23} = -\frac{m}{r} \frac{\mathbf{k} \cdot \mathbf{B}_0}{\rho_c \xi^2},\tag{58}$$

$$\xi = \omega - \frac{m}{r} v_{0\varphi}, \tag{59}$$

$$\mathbf{k} = \left(0, \frac{m}{r}, k_z\right),\tag{60}$$

$$\mathbf{B}_{0} = (0, B_{0,\varphi}, B_{0z}), \tag{61}$$

$$g_0 = d\psi_0/dr, (62)$$

$$B_{1r} = \frac{i\omega}{\xi \rho_0} \mathbf{k} \cdot \mathbf{B}_0 y_2 , \qquad (63)$$

$$\begin{pmatrix} B_{1\varphi} \\ B_{1z} \end{pmatrix} = \mathbf{T}^{-1} \mathbf{U} \begin{pmatrix} y_1 \\ y_2 \\ y_3 \\ y_4 \end{pmatrix}, \tag{64}$$

$$v_{1r} = \frac{\omega}{i\rho_0} y_1 \,, \tag{65}$$

$$\begin{pmatrix} v_{1\varphi} \\ v_{1z} \end{pmatrix} = \left[\boldsymbol{W} - \frac{\boldsymbol{k} \cdot \boldsymbol{B}_0}{4\pi\rho_0 \xi} \boldsymbol{T}^{-1} \boldsymbol{U} \right] \begin{pmatrix} y_1 \\ y_2 \\ y_3 \\ y_4 \end{pmatrix}, \tag{66}$$

$$\mathbf{W} = \begin{pmatrix} W_{11} & W_{12} & W_{13} & 0 \\ W_{21} & W_{22} & W_{23} & 0 \end{pmatrix}, \tag{67}$$

$$W_{11} = \frac{m}{r} \frac{1}{\rho_0 \xi},\tag{68}$$

$$W_{12} = -\frac{\omega}{\xi \rho_0 r} \left[\frac{d}{dr} (r v_{0\varphi}) + \frac{\mathbf{k} \cdot \mathbf{B}_0}{4\pi \rho_0 \xi} \frac{d}{dr} (r B_{0\varphi}) \right], \tag{69}$$

$$W_{13} = \frac{m}{r} \frac{1}{\xi \rho_c}, \tag{70}$$

$$W_{21} = k_z \frac{1}{\rho_0 \xi}, \tag{71}$$

$$W_{22} = -\frac{\omega \mathbf{k} \cdot \mathbf{B}_0}{4\pi\rho_0^2 \xi^2} \frac{dB_{0z}}{dr} , \qquad (72)$$

and

$$W_{23} = k_z \frac{1}{\xi \rho_c}. (73)$$

Appendix 2. The Bisection Method for Complex Eigenvalues

In this appendix we describe the method used to search for a complex eigen value. According to Paper I, the condition for an eigenvalue is expressed as

$$\chi(\omega) \equiv \det \begin{pmatrix} y_1^{(1)}(r;\omega) & y_1^{(2)}(r;\omega) & y_1^{(3)}(r;\omega) & y_1^{(4)}(r;\omega) \\ y_2^{(1)}(r;\omega) & y_2^{(2)}(r;\omega) & y_2^{(3)}(r;\omega) & y_2^{(4)}(r;\omega) \\ y_3^{(1)}(r;\omega) & y_3^{(2)}(r;\omega) & y_3^{(3)}(r;\omega) & y_3^{(4)}(r;\omega) \\ y_4^{(1)}(r;\omega) & y_4^{(2)}(r;\omega) & y_4^{(3)}(r;\omega) & y_4^{(4)}(r;\omega) \end{pmatrix} = 0,$$
(74)

where $[y_1^{(i)}, y_2^{(i)}, y_3^{(i)}, y_4^{(i)}]$ for i = 1, 2, 3, and 4 denote independent solutions satisfying either of the boundary conditions at r = 0 or ∞ . We first evaluate $\chi(\omega)$ for $\omega = \omega_1, \omega_2$, and ω_3 . The points $\omega = \omega_1, \omega_2$, and ω_3 are on the vertexes of a right isosceles triangle on the complex ω plane [see figure (13)]. We next compute

$$\eta(\omega_1 \ \omega_2 \ \omega_3) \equiv \log[\chi(\omega_1)/\chi(\omega_2)] + \log[\chi(\omega_2)/\chi(\omega_3)] + \log[\chi(\omega_3)/\chi(\omega_1)], \tag{75}$$

where each logarithm operation takes the principal value. The value of $\eta(\omega_1 \ \omega_2 \ \omega_3)$ can take either 0 or $\pm 2\pi i$. When $\eta = 2\pi i$, there is a zero point of $\chi(\omega)$ inside the triangle. Note that $\eta = \oint (1/\chi) d\chi$.

When $\eta = 2\pi i$ for the triangle $\omega_1 - \omega_2 - \omega_3$, we integrate the perturbation equation for $\omega_4 = (\omega_2 + \omega_3)/2$ and compute $\chi(\omega_4)$. Either $\eta(\omega_1, \omega_2, \omega_4)$, $\eta(\omega_1, \omega_4, \omega_3)$, or $\eta(\omega_3, \omega_4, \omega_2)$ is identical to $\eta(\omega_1, \omega_2, \omega_3)$,

$$\eta(\omega_1, \omega_2, \omega_3) = \eta(\omega_1, \omega_2, \omega_4) + \eta(\omega_1, \omega_4, \omega_3) + \eta(\omega_3, \omega_4, \omega_2). \tag{76}$$

In most cases, we obtain $\eta(\omega_3, \omega_4, \omega_2) = 0$. [The frequency of $\eta(\omega_3, \omega_4, \omega_2) \neq 0$ is very small when the triangle $\omega_1 - \omega_2 - \omega_3$ is small]. Then, the region containing the zero point of $\chi(\omega) = 0$ is reduced to half in area. The reduced region is again a right isosceles triangle and can be squeezed by successive reduction. Finally, we can obtain an eigenvalue, ω , with a sufficiently small error. Each iteration makes the estimated error smaller by a factor of $\sqrt{2}$ in this extended bisection method.

REFERENCES

Balbus S. A., Hawley, J. H. 1991, ApJ 376, 214

Bally J. 1989, in Low Mass Star Fromation and Premain Sequence Objects, ed Reipurth B. (ESO, Garching) p1

Bonnell I., Arcoragi J.-P., Martel H., Bastien P. 1992, ApJ 400, 579

Chandrasekhar S., Fermi E. 1953, ApJ 118, 116

Fujimoto M. Y. 1987, A&A 176, 53.

Glatzel W. 1987a, MNRAS 225, 227

Glatzel W. 1987b, MNRAS 228, 77

Habe A., Uchida Y., Ikeuchi S., Pudritz R.E. 1991, PASJ 43, 703

Hanawa T. 1986, MNRAS 223, 859

Hanawa T. 1987, A&A 179, 383

Hanawa T., Nakamura F., Matsumoto T., Nakano T., Tatematsu K., Umemoto T., Kameya O. et al. 1993, ApJL 404, L83

Hansen C. J., Aizenman M. L., Ross R. R. 1976, ApJ 207, 736

Inutsuka S., Miyama S. M. 1992, ApJ 388, 392

Kato S. 1987, PASJ 39, 645

Lin C. C. 1945a, Quart. Appl. Math. 3, 117

Lin C. C. 1945b, Quart. Appl. Math. 3, 218

Moneti A., Pipher J. L., Helfer H. L., McMillan R. S., Perry M. L. 1984, ApJ 282, 508

Nagasawa M. 1987, Prog. Theor. Phys. 77, 635

Nakamura F., Hanawa T., Nakano T. 1993, PASJ 45, 551 (Paper I)

Olano C. A., Walmsley C. M., Wilson T. L. 1988, A&A 196, 194

Ostriker J. 1964, ApJ 140, 1056

Stodołkiewicz J. S. 1963, Acta Astron. 13, 30

Sung C. H. 1974, A&A 33, 99.

Tatematsu K., Umemoto T., Kameya O., Hirano N., Hasegawa T., Hayashi M., Iwata T., Kaifu N. et al. 1993, ApJ 404, 643

Tomisaka K. 1993, ApJ submitted to

Uchida Y., Fukui Y., Minoshima Y., Mizuno A., Iwata T., Takaba H. 1991, Nature 349, 140

Vrba F. J., Strom S. E., Strom K. M. 1976, AJ 81, 958

This preprint was prepared with the AAS IATEX macros v3.0.

- Fig. 1.— Dispersion relation for models with $(\alpha, \beta) = (0, 1)$. The thick curve denotes the growth rate, ω_i , as a function of the wavenumber, k_zH . The thin and dashed curves denote the growth rate of the most unstable mode with $(\alpha, \beta, \theta) = (1, 0, 0^{\circ})$ and $(0, 0, 0^{\circ})$, respectively, for comparison.
- Fig. 2.— Dependence of the growth rate, ω_i , of the sausage (m=0) mode on β for $\alpha=0$. Each curve denotes the growth rate of the unstable sausage mode with $(\alpha, \beta) = (0, 0), (0, 1),$ and (0, 2). The ordinate is the growth rate, ω_i , and the wave number, k_z .
- Fig. 3.— Wave number of the most unstable perturbation as a function of $\alpha + \beta$ for $\theta = 0^{\circ}$. The ordinate and abscissa of the upper panel are the wavenumbers of the most unstable perturbation, $k_{\text{max}}H$ and $\alpha + \beta$, respectively. The filled circles denote the numerically obtained data points, and the curve denotes the fitting formula, equation (22). The lower panel shows the error of the fitting formula. The ordinate is (error) \equiv (fitting formula)/(numerical data) -1.
- Fig. 4.— Cross section of the model filamentary cloud perturbed by the fastest growing sausage mode (main panel). The model parameters of the equilibrium model are $(\alpha, \beta, \theta) = (0, 1, 0^{\circ})$. The abscissa is the z-axis and the ordinate is the radial direction. The density is indicated by greyness, the scale of which is shown on the left side of the panel. The arrows denote the velocity field on the r-z plane. The right-hand panel shows v_{φ} as a function of r at z=0.0. The dashed and solid curves denote the values in equilibrium and in the perturbed state, respectively. The growth rate and the wave number of this perturbation are $\omega_i = 0.606$ and $k_z = 0.467$, respectively.
- Fig. 5.— Same as figure 4, but for $(\alpha, \beta, \theta) = (0.5, 0.5, 0^{\circ})$. The growth rate and the wave number of this perturbation are $\omega_i = 0.640$ and $k_z = 0.478$, respectively.
- Fig. 6.— Dispersion relation of the kink (m=1) mode for $(\alpha, \beta) = (0, 1)$. The dashed and solid curves denote ω_r and ω_i , the oscillation frequency and growth rate, respectively. The three horizontal dotted lines denote the angular velocities, Ω , at r=2, $2\sqrt{2}$, and 4,respectively.
- Fig. 7.— Same as figure 6, except for $(\alpha, \beta) = (0, 0.5)$.
- Fig. 8.— Same as figure 6, except for $(\alpha, \beta) = (0, 2)$.
- Fig. 9.— Same as figure 4, except for the most unstable kink mode with $(\alpha, \beta) = (0, 1)$. The wave number and growth rate are $Hk_z = 0.323$ and $\omega_{i, \text{max}} = 0.135 \sqrt{(2\pi G \rho_c)}$, respectively. The amplitude of the perturbation is normalized so that $\rho_1/\rho_c = 0.5$ at maximum. (a) The cross section in the r-z plane. (b) The cross section of z=0.
- Fig. 10.— Same as figure 6, except for the kink mode of $(\alpha, \beta, \theta) = (0.5, 0.5, 0^{\circ})$.

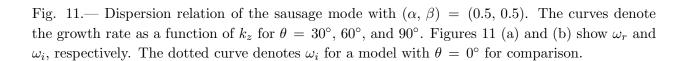


Fig. 12.— Same as figure 4, except for the sausage mode with $(\alpha, \beta, \theta) = (0.5, 0.5, 60^{\circ})$. The growth rate and wave number are $\omega = (0.0199 + 0.594 i) \sqrt{(2\pi G\rho_c)}$ and $k_z H = 0.432$, respectively.

Fig. 13.— Search for a complex eigenvalue on the complex ω plane. The region for the search narrows by a factor of 2 in area by each iteration.